Available online at www.sciencedirect.com
SCIENCE DIRECT®
Physica D 195 (2004) 207–228
PHYSICA D
www.elsevier.com/locate/physd

# Blown by wind: nonlinear dynamics of aeolian sand ripples

Hezi Yizhaq[a,b], Neil J. Balmforth[c,d], Antonello Provenzale[e,f,*]

[a] *ISI Foundation, V.le. Settimio Severo 65, I-10133 Turin, Italy*
[b] *BIDR, Ben Gurion University, Sede Boker Campus 84990, Israel*
[c] *Department of Applied Mathematics and Statistics, UCSC, Santa Cruz, CA 95064, USA*
[d] *Department of Mathematics and Earth and Ocean Sciences, University of British Columbia, Vancouver, BC, Canada*
[e] *ISAC-CNR, Corso Fiume 4, I-10133 Turin, Italy*
[f] *CIMA, University of Genoa, I-17100 Savona, Italy*

Received 28 March 2003; received in revised form 16 March 2004; accepted 18 March 2004
Communicated by C.K.R.T. Jones

**Abstract**

A nonlinear continuum model is considered that describes the dynamics of two-dimensional aeolian sand ripples. This integro-differential model is based on a phenomenological approach due to Anderson. Linear stability analysis using this model shows that a flat sand bed exposed to the action of wind is linearly unstable to long-wavelength perturbations. As the ripples grow, nonlinear effects become important, ripples become asymmetric and the wavelength increases due to merging events. A long-wavelength approximation to the full integral model is then derived. The ripple field produced by the long-wave theory undergoes coarsening, drifts downwind and displays bifurcations and defects which move from one ripple to another, similar to what is observed for sand ripples in the desert.


*PACS:* 81.05.Rm; 83.70.Fn; 47.20.−k

*Keywords:* Aeolian sand ripples; Pattern formation; Geomorphology

## 1. Introduction

Aeolian ripples are commonly found in sand deserts on the Earth and Mars [1–3]. Fig. 1 shows the pictures of aeolian sand ripples in the desert of the Great Sand Dunes National Monument in Colorado (upper panel) and in the Wadi Rum desert in Jordan (lower panel). Ripple wavelengths typically range from a few centimetres to tens of meters, and ripple amplitudes range from a few millimetres to a maximum of a few centimetres. The "ripple index", defined as the ratio of the ripple height to wavelength, usually ranges between 15 and 20, with a standard value of 18 for sand ripples and 15 for granule ripples. Ripple profiles are slightly asymmetric, with the downwind slope slightly steeper than the upwind slope. The asymmetry of ripple profiles is much less pronounced than for dunes, for which the downwind slope is usually at the angle of repose for sand. A classic reference to the phenomenology

* Corresponding author. Fax: +39-011-6600364.
*E-mail addresses:* yiyeh@bgumail.bgu.ac.il (H. Yizhaq), njb@ams.ucsc.edu (N. J. Balmforth), a.provenzale@isac.cnr.it (A. Provenzale).

0167-2789/$ – see front matter © 2004 Published by Elsevier B.V.
doi:10.1016/j.physd.2004.03.015

Fig. 1. Upper photo: sand ripples at Great Sand Dunes National Monument in Colorado (photograph by Bob Bauer). The foreground (lower part of the picture) shows sand ripples which exhibits a typical fingerprint-like pattern. The background (upper part of the picture) shows granule ripples with wavelength up to 2 m and height up to 9 cm [3]. Lower photo: sand ripples atop a dune in the Wadi Rum desert in Jordan. The wavelength is about 10–15 cm and the height is a few mm.

and the dynamics of ripples and dunes is the book "The Physics of Blown Sand and Desert Dunes" by R.A. Bagnold [1]. Detailed descriptions of the properties of aeolian ripples are provided in [4–8].

The physical mechanism responsible for the formation of aeolian ripples is thought to be the action of wind on loose sand. When the wind strength is large enough, individual sand grains are lifted by the direct action of the shear stress exerted by the wind on the sand surface. Even for strong winds, however, sand grains are too heavy to stay suspended and return to the ground. During their flight, the grains reach a velocity that is approximately that of the wind, and, upon their impact with the surface, they impart their energy and momentum to the sand, and eject other grains. For sufficiently large wind velocities, the bombardment by sand grains accelerated by the wind generates a cascade process, and an entire population of saltating grains hopping on the sand surface emerges [35]. During strong winds, the layer of saltating grains can reach a thickness of more than 1 m.

Mathematical models of ripple dynamics date back to the work of Bagnold [1]. The original idea of Bagnold was based on the existence of "a rhythmic barrage of grains" that jump from one ripple crest to another, in what is called the "ballistic hypothesis" [7]. The ballistic hypothesis was questioned by Bagnold himself, and it was later abandoned because experimental observations showed that grains jump over distances that are much larger than the ripple wavelength [9]. Moreover, this model cannot predict the merging of ripples and the resulting "coarsening" of ripple patterns that is observed in natural settings [4].

Other explanations of ripple emergence were based on so-called "wave hypotheses". In one approach, the sand layer was considered as a fluid on which waves could propagate [10]. This explanation is now dismissed because there is no evidence of sand motion inside the sand bed itself. Other versions of the wave hypotheses considered the effect of wave-like perturbations in the dusty overlying air [11,12]. Although these possibilities cannot be ruled out, at present there is not much empirical evidence to support them.

A significant advance in the theoretical understanding of ripple formation was achieved thanks to the work of Anderson [13,14]. His approach was based on the experimental observation that bombardment generates two populations of moving grains [15]: grains that are ejected with large energy form the population of "saltating" grains. These grains reach higher elevations and are directly accelerated by the wind. The second population consists of grains that are ejected with low energy, and stay close to the sand surface. These crawling grains form what is called the "reptating" population. Low-energy grains typically jump to a distance that is up to a few tens of the average grain size [32], and may continue to roll on the sand surface after landing. The exchange flux between the reptating and the saltating populations is thought to be small [13].

In Anderson's model [13,14], the only role of saltating grains is to bring energy into the system, having extracted it from the wind. The saltating grains energise the reptating population, and ripple formation is entirely due to the spatial variability of the flux of reptating grains. Anderson's original model deals with a two-dimensional layer of sand, i.e. one-dimensional ripples, and formulates the problem in terms of an integro-differential equation describing the one-dimensional sand surface. The dynamics of the reptating grains is handled by a probabilistic approach in which the grains take steps of random length, which avoids tracking the detailed dynamics of the impact and reptation flight. In the model, ripples arise as a linear instability of a uniform layer of sand. One physically unappealing feature of the model is that, in the linear stability theory, large wavenumbers remain linearly unstable.

In this work, we generalise Anderson's model, making two significant modifications. First, we add the third dimension and consider ripples as fully two-dimensional structures on the sand surface. To incorporate the third dimension, we allow the reptating grains to not only take steps of random length, but also to be scattered away from the direction of the incoming saltating grains at random angles. As in Anderson's original model, the total reptating flux is obtained from an ensemble average over the distributions from which the random angles and step lengths are drawn. To our knowledge, this is the first continuum model for two-dimensional ripples reported in the literature.

Our second modification of Anderson's model is to introduce a phenomenological correction to the reptation flux that makes it slightly smaller on the windward (stoss) slope and slightly larger on the lee slope, in agreement with observations and numerical simulations [16,17]. This correction stabilises the short wavelengths and shifts the maximum of the reptation flux closer to the ripple crest, stopping excessive growth of the model ripples [5]. Following Prigozhin [17], we introduce the correction by arguing that the inclination of the sand surface foreshortens or lengthens the paths of reptating particles. However, the form of the correction is also similar to phenomenological models of the flux due to rolling grains [18].

We also note that there has been a recent resurgence of interest in developing mathematical models of the dynamics of aeolian ripples, a fact that has led to a series of papers based on different types of phenomenological and mathematical assumptions [16,17,19–30]. Some of these works are based on discrete modelling approaches, such as cellular automata, and include empirical rules of sand grain behaviour [16,20,43]. Such a phenomenological approach allows for considering populations of sand grains with different size and for including effects that are not

easily described by a continuum model; it has the disadvantage that it makes little or no direct use of the physical rules that govern grain dynamics.

One continuum model is based on the mathematical implementation of Bagnold's idea on the rythmic barrage of grains [19]. This type of approach can be questioned for the same reasons that suggested to abandon Bagnold's hypothesis on ripple formation. Another type of continuum model is based on the extension of Anderson's approach by the explicit description of the rolling and avalanching of sand grains due to gravity [23]. Explicit consideration of the dynamics of rolling grains and of the saltation flux is at the core of still another family of continuum models based on the extension of the so-called BCRE equations for granular media [31]. This approach describes the joint dynamics of the sand surface elevation and of the surface density of moving sand particles, leading to a two-equation system [17,26]. The advantage of these models is the explicit inclusion of the dynamics of moving grains, which is parameterised in the simpler Anderson's type model. A disadvantage of these models is a higher level of complication and the need for more phenomenological parameters and functional dependencies. Weakly nonlinear approximations to some of these models [26] lead to a long-wave equation that displays coarsening dynamics. To our knowledge, none of these models has been extended to two horizontal dimensions. See [26] for a longer discussion of some of these continuum models.

The approach followed here is different in that it is directly based on the phenomenological description developed by Anderson [13]. As we show below, this simple model, when properly treated, is capable of describing, at least qualitatively, many of the properties of aeolian sand ripples. Interestingly, the long-wave expansion of this model leads to an equation that is equivalent to those that can be derived from some of the more complicated models. In addition, thanks to its simplicity, this model is easily extended to describe the dynamics of two-dimensional ripples.

In Sections 2 and 3 we derive our model and present a linear stability theory that predicts an instability in the form of undulations in the direction of the wind, with little transverse variation. Section 4 describes a long-wave analysis of the model based on the fact that the instability invariably has long spatial scale in both directions. The long-wave theory has a form dictated by the symmetries of the problem [26,28], and the original model fixes only the values of a set of coefficients, which makes that theory common to a variety of ripple-forming models. Section 5 sets the stage for a discussion of the nonlinear dynamics by first exploring the one-dimensional version of the theory; we compare numerical solutions of the integro-differential model with analogous results from the long-wave theory, and confirm the validity of that theory even in the nonlinear regime. We present some new results on the coarsening of nonlinear ripples. Section 6 presents solutions for two-dimensional ripples using the long-wave theory, and in Section 7 we offer a summary and conclusions.

## 2. The integro-differential model

### 2.1. Saltation and reptation fluxes

We base our model of sand transport by wind on the so-called Exner equation, expressing the conservation of sand:

$$(1-\lambda_p)\rho_p \frac{\partial \zeta}{\partial t} = -\nabla \cdot \mathbf{Q}, \tag{1}$$

where $\zeta(x,t)$ is the local height of the sand surface at point $x$ and time $t$, $\rho_p$ is the density of a sand grain, $\lambda_p$ is the porosity of the bed (typically taken as 0.35), and $\mathbf{Q}(x,t)$ is the horizontal sand flux. This equation shows that erosion (deposition) occurs in regions where the sediment flux is diverging (converging), and there is no change in the surface height where the transport rate is constant.

In principle, the total sand flux is obtained as the sum of the flux of saltating grains and that of reptating grains, $\mathbf{Q} = \mathbf{Q}_s + \mathbf{Q}_r$. Saltating grains are accelerated by the wind to speeds that are close to the wind speed. These grains follow a ballistic path to the next impact site. If their arced trajectory is long compared to the size of the bed undulations, it seems plausible that the angle at which the grains descend back to the bed is dictated largely by the wind. Thus, following Anderson and others, we assume that the ballistic, wind-buffeted trajectory of a saltating particle leaves that grain with no memory of its initial ejection, and all grains descend at a fixed angle and with a fixed speed. We take the wind to blow in the $x$-direction, which also then sets the direction of the incoming flux of saltating grains. On average, the flux of saltating grains, $\mathbf{Q}_s$, can thus be taken as spatially constant and discarded from the Exner equation ($\nabla \cdot \mathbf{Q}_s = 0$). This basic simplification, introduced by Anderson [13], is probably not tenable for larger bedforms such as dunes and megaripples. In these latter cases, the spatial variability of the flux of saltating grains, as well as the feedback of the bedform on the sand flux, must be taken into account [33,34].

The mass flux of reptating grains at a given point $x$ and time $t$, $\mathbf{Q}_r$, is obtained by summing over all the grains that are still in flight and are passing by that point at that time. If all the grains had the same reptation length $\alpha$, the flux at $(x, y)$ in the direction at angle $\psi$ to the $x$-axis would be proportional to the number of grains that have been ejected between $(x-\alpha\cos\psi,\ y-\alpha\sin\psi)$ and $(x, y)$ and were travelling in that particular direction (note that this introduces a basic non-locality in the dynamics of aeolian ripples). In reality, the grains have a distribution of reptation lengths and are scattered at varying angles to the wind direction. Our crude model does not follow the detailed paths of the saltating and reptating grains and we model the uncertainty in the grain dynamics probabilistically. We assume that the impact of a saltating grain generates a flux of reptating grains each of which takes a step with a random length, $A$, in a direction given by a random angle, $\Psi$, with the $x$-direction. The random variables, $A$ and $\Psi$, have the joint probability density, $p_{A,\Psi}(a, \psi)$, which is the two-dimensional analogue of the "splash function" of Ungar and Haff [35]. This joint distribution is currently not known, either from experiments or theory, but must be fed into the theory as an arbitrary function. However, we do impose the physically sensible restriction that $\rho_{A,\Psi}(a, \psi)$ is left–right symmetric: $\rho_{A,\Psi}(a, -\psi) = \rho_{A,\Psi}(a, \psi)$. Later we also take $A$ and $\Psi$ to be independent, in which case $p_{A,\Psi}(a, \psi) = p_A(a)\,p_\Psi(\psi)$.

Now, the flux of reptating particles through the point $(x, y)$ that are scattered in the direction $\psi$ and take a step length of $a$ is

$$nm\int_0^a N_{im}(x - r\cos\psi,\ y - r\sin\psi)\,\mathrm{d}r\,\hat{\mathbf{r}}, \tag{2}$$

where $m$ is the mass of each particle, $n$ is the average number of reptating grains, per unit surface area and unit time, that are ejected by the impact of one saltating grain, and $\hat{\mathbf{r}} = (\cos\psi,\ \sin\psi)^{\mathrm{T}}$. The value of $n$ could depend on the impact velocity, on the diameter of the grains [36–38] and possibly on the bed slope [32]; however, in our model we assume $n$ to be constant.

Performing the ensemble average over all angles and step lengths gives the total flux:

$$\mathbf{Q}_r = nm\int_0^\infty\int_{-\pi}^{\pi} p_{A,\Psi}(a, \psi)\,\mathrm{d}a\,\mathrm{d}\psi\int_0^a N_{im}(x - r\cos\psi,\ y - r\sin\psi)\,\mathrm{d}r\,\hat{\mathbf{r}}, \tag{3}$$

or

$$\mathbf{Q}_r = nm\left\langle\int_0^a N_{im}(x - r\cos\psi,\ y - r\sin\psi)\,\mathrm{d}r\,\hat{\mathbf{r}}\right\rangle, \tag{4}$$

on denoting the ensemble average by angular brackets. Note that, by putting $p_{A,\Psi}(a, \psi) = p(a)\delta(\psi)$, we recover Anderson's model flux.

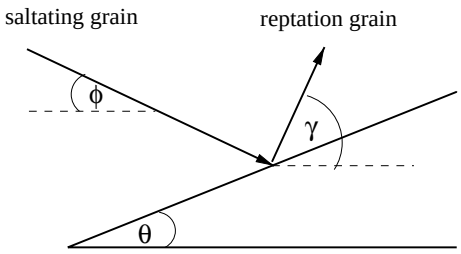


Fig. 2. Illustration of a typical collision process. All angles are referred to a horizontal surface. A saltating grain approaches the inclined bed at angle $\phi$. A reptating grain is ejected at angle $\gamma$. The inclination of the bed is $\theta$ ($\theta$ is positive on the windward slope). The saltating grain ricochets (not shown in the figure) and continues the cascade.

Lastly, we must specify $N_{im}$. Although the incoming saltation flux is assumed to be uniform and fixed in direction, the inclination of the sand surface modifies the number density of impacting grains through projection. Geometrical considerations indicate that

$$N_{im} = N_{im}^0 \cot\phi \frac{\tan\phi + \zeta_x}{\sqrt{1+\zeta_x^2+\zeta_y^2}} \equiv N_{im}^0 \cot\phi F(x, y), \tag{5}$$

where $N_{im}^0$ is the number density of impacting grains on a flat horizontal surface (cf. Fig. 2). Eq. (5) formally breaks down when $\tan\phi + \zeta_x < 0$, which arises when the lee slope of the ripples exceeds the impact angle $\phi$ of the saltating grains. In such situations, the ripples are sufficiently steep to cast a shadow. To avoid the unphysical negative flux predicted by (5), we impose the positivity constraint:

$$F(x, y) = \frac{\mathrm{Max}(\tan\phi + \zeta_x, 0)}{\sqrt{1+\zeta_x^2+\zeta_y^2}}. \tag{6}$$

Note, however, that shadowing is a truly non-local effect and the constraint above should be taken only as a local approximation that describes one of the main effects.

### 2.2. Slope-modified steps

Next, we incorporate corrections that account for a mild dependence of the reptation step on the local topography (cf. [17]). When a reptating grain is scattered from an impact, it is launched above the sand surface with an initial velocity, $V$, and angle to the horizontal, $\gamma$. On a horizontal surface, these dictate the step length $a$, but for our evolving landscape the step is foreshortened or lengthened by the change in elevation of the point where the grain returns to the surface. Provided the reptation length is small, the landscape can be locally approximated by a plane of slope $\vartheta$. Then, it is straightforward to show that the step in the horizontal is given by

$$2\frac{V^2}{g}\frac{\sin(\gamma-\vartheta)\cos\gamma}{\cos\vartheta} \equiv a(1 - \tan\vartheta\cot\gamma), \tag{7}$$

where $a$ is now the step that would have been taken on a flat plane and $g$ is the acceleration of gravity. Now, the local slope is determined by the direction taken by the scattered grain, $\psi$ : $\tan\vartheta \equiv \zeta_x\cos\psi + \zeta_y\sin\psi$. Hence, a step modification factor, $f$, can be introduced, with $f = 1 - (\zeta_x\cos\psi + \zeta_y\sin\psi)\cot\gamma$. This correction shortens the mean reptation length on the windward slope of the bedform and lengthens it on the leeward slope, as seen in numerical simulations (see Fig. 5 in [16]).

The flux of reptating particles through $(x, y)$ is now modified to

$$\mathbf{Q}_{\mathrm{r}} = \frac{nmN_{im}^{0}}{\tan\phi}\left\langle \int_{0}^{af} F(x - r\cos\psi,\, y - r\sin\psi)\,\mathrm{d}r\,\hat{\mathbf{r}}\right\rangle, \tag{8}$$

or

$$\mathbf{Q}_{\mathrm{r}} = \frac{nmN_{im}^{0}}{\tan\phi}\left\langle f\int_{0}^{a} F(x - fr'\cos\psi,\, y - fr'\sin\psi)\,\mathrm{d}r'\hat{\mathbf{r}}\right\rangle. \tag{9}$$

At this stage, we should also include an integral over all the possible elevation angles $\gamma$ (with a suitable probability distribution). However, to avoid the resulting expression from being too cumbersome (which seems unwarranted given the crudeness of the theory), we approximate the flux by ignoring the small correction that enters from the step modification within the arguments of $F$. That is, we make the replacement $f = 1$ inside the integrand of (9). The average over all possible $\gamma$ is therefore only taken in the prefactor of the $r$-integral in (9), and there we denote the average of $\cot\gamma$ by a parameter, $\mu$. Thence:

$$\mathbf{Q}_{\mathrm{r}} = \frac{nmN_{im}^{0}}{\tan\phi}\left\langle [1 - \mu(\zeta_x\cos\psi + \zeta_y\sin\psi)]\int_{0}^{a} F(x - r'\cos\psi,\, y - r'\sin\psi)\,\mathrm{d}r'\hat{\mathbf{r}}\right\rangle. \tag{10}$$

Note that the factor $f$ inside the integrand of $(g)$ can be safely ignored in linear stability analysis because it enters nonlinearly, in contrast to the linear term stemming from the pre-factor. In a fully nonlinear description, discarding the factor $f$ in the integrand must be taken as a phenomenological approximation.

As with the cut-off for $F(x, y)$ in (10), we should limit the correction factor, $f$, to be positive to prevent a negative flux. This happens when the slope is so steep in a particular direction that it is impossible to scatter reptating grains that way. To avoid excessively cluttering the formulae, we assume that this never happens.

For the one-dimensional problem, the slope modification to the step length provides a multiplicative flux correction of the form $1 - \mu\zeta_x$, similar to the correction introduced by Prigozhin in the context of a two-species model where the rolling of particles upon the sand surface and the action of the wind are dealt with separately [17]. In fact, this kind of correction factor has also been postulated by Hardisty and Whitehouse [18] to account for a completely different physical process, an "impact-induced gravity flow". In this instance, $\mu \equiv \cot\theta_{\mathrm{r}}$, where $\theta_{\mathrm{r}}$ is the angle of repose. In other words, although we add the parameter $\mu$ as a model of the slope modification to the step length, it also crudely models several other phenomena. We leave the value of $\mu$ open, taking it as a free parameter of the model. The value could be determined empirically, provided this kind of parameterisation offers a qualitatively correct description of the processes that are not explicitly taken into account in the model and folded heuristically into $\mu$.

### 2.3. The model

We now write the explicit form of the Exner equation, given the reptation flux:

$$\zeta_t = -Q_0\left\langle \int_{0}^{a} \hat{\mathbf{r}}\cdot\nabla[(1 - \mu\zeta_x\cos\psi - \mu\zeta_y\sin\psi)F(x - r'\cos\psi,\, y - r'\sin\psi)]\,\mathrm{d}r'\right\rangle, \tag{11}$$

where $Q_0 = N_{im}^{0}mn\cot\phi/[\rho_{\mathrm{p}}(1 - \lambda_{\mathrm{p}})]$.

Finally, it is helpful to place (11) in a dimensionless form: we define $x = \alpha\tilde{x}$, $y = \alpha\tilde{y}$, $a = \alpha\tilde{a}$, $r' = \alpha\tilde{r}$, $\zeta = \alpha\tilde{\zeta}$ and $t = \alpha\tilde{t}/Q_0$, where $\alpha$ is the mean step length of reptating grains on the horizontal surface. After dropping the tilde decoration, the governing equation becomes

$$\zeta_t = -\left\langle \int_{0}^{a} \hat{\mathbf{r}}\cdot\nabla\left[(1 - \mu\zeta_x\cos\psi - \mu\zeta_y\sin\psi)F(x - r\cos\psi,\, y - r\sin\psi)\right]\mathrm{d}r\right\rangle. \tag{12}$$

## 3. Linear stability analysis

The model admits a steady solution in the form of a flat bed. We test the linear stability of this equilibrium by introducing the solution, $\zeta = Z\,\mathrm{e}^{\mathrm{i}kx+\mathrm{i}ly+\lambda t}$, into the governing equation, and dropping nonlinear terms in the amplitude, $Z$. Then

$$\lambda = \left\langle \int_0^a \mathrm{d}r' q(k\,\mathrm{e}^{-\mathrm{i}qr'} - \nu q) \right\rangle, \tag{13}$$

where $q = k\cos\psi + l\sin\psi$ and $\nu = \mu\tan\phi$. Performing some integrals:

$$\lambda = \mathrm{i}k\langle \mathrm{e}^{-\mathrm{i}aq}\rangle - \mathrm{i}k - \nu(k^2\langle a\,\cos^2\psi\rangle + l^2\langle a\sin^2\psi\rangle) \tag{14}$$

(on demanding that the angular probability distribution is symmetrical left–right).

### 3.1. Two sample distributions

To go further, we assume $\Psi$ and $A$ are independent, so $p_{A,\Psi}(a,\psi) = p_A(a)p_\Psi(\psi)$, and then introduce the Fourier series decomposition:

$$p_\Psi(\psi) = \frac{1}{2\pi} + \sum_{n=1}^{\infty} b_n \cos n\psi, \tag{15}$$

where the coefficients can be chosen to model specific angular distributions. Examples are shown in Fig. 3.

The averages in (14) are computed as follows:

$$\langle a\,\cos^2\psi\rangle = \tfrac{1}{2}(1+\pi b_2), \qquad \langle a\sin^2\psi\rangle = \tfrac{1}{2}(1-\pi b_2) \tag{16}$$

and

$$\langle \mathrm{e}^{-\mathrm{i}aq}\rangle = \int_0^\infty J_0(\kappa a)\,p_A(a)\,\mathrm{d}a + \sum_{n=1}^{\infty} 2\pi(-\mathrm{i})^n b_n \cos n\varphi \int_0^\infty J_n(\kappa a)\,p_A(a)\,\mathrm{d}a, \tag{17}$$

where $J_n(x)$ denotes a Bessel function, $\varphi = \tan^{-1}(l/k)$ and $\kappa^2 = k^2 + l^2$.

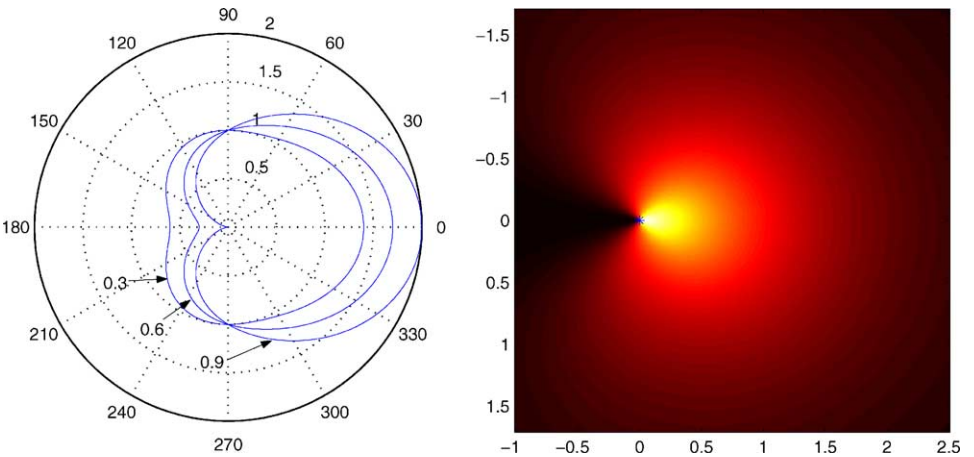


Fig. 3. Sample probability distributions. The polar plot show three angular distributions described by (15) with $b_n = 0$ for $n \neq 1$ and 3, $2\pi b_3 = 0.1$ and three values of $b_1$ ($2\pi b_1 = 0.3$, 0.6 and 0.9). The third case is shown also in the second plot, which combines that angular distribution with the exponential step-length distribution, $p_A(a) = \mathrm{e}^{-a}$, and plots $p_{A,\Psi}(a,\psi)$ as a density over the corresponding Cartesian plane; the star at the origin marks the impact site.

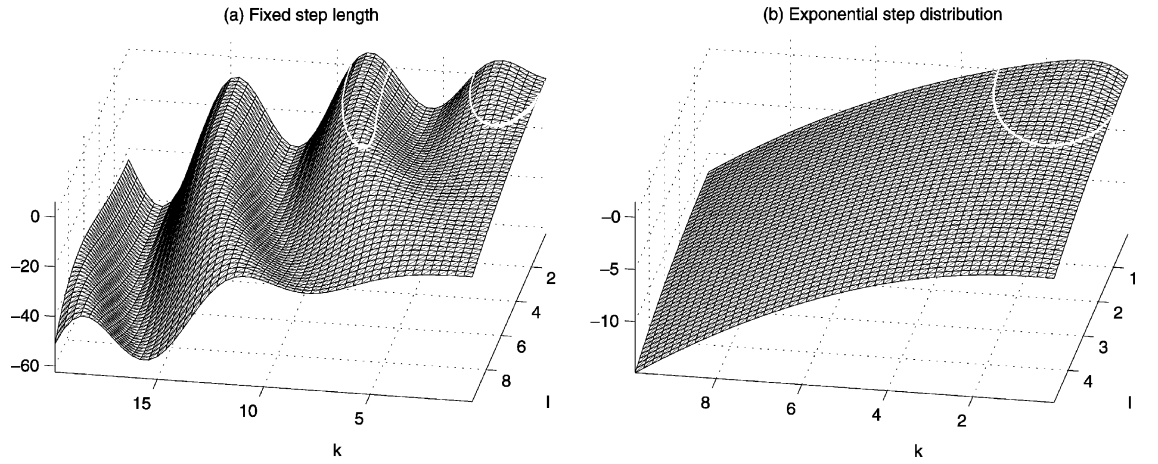


Fig. 4. Growth rate as a surface above the $(k, l)$-plane for (a) fixed step length, and (b) the exponential step distribution. The angular distribution is given by (15) with $b_n = 0$ for $n \neq 1$ and 3, $2\pi b_3 = 0.1$ and $2\pi b_1 = 0.9$. In both cases, $\nu = \mu \tan\phi = 1/4$. The break in the surfaces shows the curve of neutral stability.

For a fixed step length, $p_A(a) = \delta(a - 1)$, and the dispersion relation becomes

$$\lambda = \mathrm{i}k \left[ J_0(\kappa) - 1 + \sum_{n=1}^{\infty} 2\pi(-\mathrm{i})^n b_n \cos n\varphi J_n(\kappa) \right] - \frac{1}{2}\nu[k^2(1 + \pi b_2) + l^2(1 - \pi b_2)]. \tag{18}$$

The growth rate, $\lambda_\mathrm{r} = \mathrm{Re}(\lambda)$, is illustrated in Fig. 4 for the angular distribution of Fig. 3, with $2\pi b_1 = 0.9$ and $\nu = \mu \tan\phi = 1/4$.

A more realistic step-length distribution is the exponential, $p_A(a) = \mathrm{e}^{-a}$, for which:

$$\lambda = \mathrm{i}k \sum_{n=1}^{\infty} b_n \cos n\varphi \int_{-\pi}^{\pi} \frac{\cos n\psi \, \mathrm{d}\psi}{1 + \mathrm{i}\kappa \cos\psi} - \mathrm{i}k - \frac{1}{2}\nu[k^2(1 + \pi b_2) + l^2(1 - \pi b_2)]. \tag{19}$$

The growth rate is also illustrated in Fig. 4 for the same angular probability model and parameter values.

From Fig. 4, we observe that the slope-dependent correction of the flux stabilises the shorter wavelengths. The destabilisation effect of the varying reptation flux must compete and overcome this stabilisation for ripples to become unstable. Note that low impact angles favour destabilisation of the bed because stabilisation is controlled by the parameter $\nu = \mu \tan\phi$.

### 3.2. Long-wave instability

For both examples of splash function, the instability has a long-wave character (the case with fixed step length may acquire more unstable windows at higher wavenumber, but the low-wavenumber window is most difficult to stabilise on raising $\nu$). Should this remain true for all reptation probability distributions, we may extract a general analytical stability criterion using a long-wave expansion. We set $k = \epsilon K$ and $l = \epsilon^2 L$, where $\epsilon \ll 1$. Then

$$\langle \mathrm{e}^{-\mathrm{i}Ka} \rangle \to 1 - \mathrm{i}\epsilon K \langle a \cos\psi \rangle - \tfrac{1}{2}\epsilon^2 K^2 \langle a^2 \cos^2\psi \rangle + \tfrac{1}{6}\mathrm{i}\epsilon^3 K^3 \langle a^3 \cos^3\psi \rangle + \mathrm{O}(\epsilon^4) \tag{20}$$

(again using symmetry), leading to the growth rate:

$$\lambda_r \to \epsilon^2 K^2(\langle \cos\psi\rangle - \nu\langle \cos^2\psi\rangle) - \epsilon^4 L^2 \nu\langle \sin^2\psi\rangle - \tfrac{1}{6}\epsilon^4 K^4\langle a^3\ \cos^3\psi\rangle + \mathrm{O}(\epsilon^6)$$
$$\sim \epsilon^2 K^2[\pi b_1 - \tfrac{1}{2}\nu(1+\pi b_2)] - \tfrac{1}{2}\epsilon^4 L^2\nu(1-\pi b_2) - \tfrac{1}{24}\pi\epsilon^4 K^4\langle a^3\rangle(3b_1+b_3). \tag{21}$$

Thus, stability is assured if

$$\langle \cos\psi\rangle < \nu\langle \cos^2\psi\rangle \quad \text{or} \quad 2\pi b_1 < \mu(1+\pi b_2)\tan\phi \tag{22}$$

and we observe immediately what properties of the probability distribution (the lowest-order moments of the angular distribution) dictate stability. Finally, diffusion in the transverse direction clearly plays a stabilising role.

## 4. A compact, or minimal, long-wave model

As seen above, the linear theory is explored analytically on focussing on long waves. However, one can proceed further with such an expansion, and derive a long-wave model for the nonlinear dynamics. In performing such an expansion, the details of the original equations become collected into the coefficients of a standard type of equation whose form is otherwise dictated by the symmetries of the problem. This notion was used by Csahók [26] and Balmforth et al. [28] to pass from crude one-dimensional models to a certain long-wave model. The argument in favour of the latter is that it corresponds to the long-wave limit of many different original formulations, and so offers a compact description of the dynamics independently of some of the differing physical details (those differences simply amount to varying choices of the values of the parameters in the long-wave equation).

To derive a long-wave equation, we again introduce the small parameter $\epsilon$, and then rescale the space and time coordinates: $X = \epsilon x$, $T = \epsilon^2 t$ and $Y = \epsilon^2 y$. The governing equation is thus rewritten as

$$\epsilon\zeta_T = -\left\langle \int_0^a \mathrm{d}r(J_X\cos\psi + \epsilon J_Y \sin\psi)\right\rangle, \tag{23}$$

where

$$J = (1-\epsilon\mu\zeta_X\cos\psi - \epsilon^2\mu\zeta_Y\sin\psi)\left[\frac{\tan\phi+\epsilon\zeta_X}{\sqrt{1+\epsilon^2\zeta_X^2+\epsilon^4\zeta_Y^2}}\right]_{X-\epsilon r\cos\psi, Y-\epsilon r\sin\psi}. \tag{24}$$

Taylor expanding the un-averaged flux to order $\epsilon^3$:

$$J \sim \tan\phi + \epsilon\zeta_X(1-\nu C) - \epsilon^2(r\zeta_{XX}C + \tfrac{1}{2}\zeta_X^2\tan\phi + \nu\zeta_Y S + \mu\zeta_X^2 C)$$
$$+\epsilon^3[(\mu C + \tan\phi)r\zeta_X\zeta_{XX}C + \tfrac{1}{2}\nu\zeta_X^3(\nu C-1) - \mu\zeta_X\zeta_Y S + \tfrac{1}{2}r^2\zeta_{XXX}C^2 - r\zeta_{XY}S], \tag{25}$$

where we have introduce the short-hand notation, $S = \sin\psi$ and $C = \cos\psi$. Each term can be integrated in $r$, and then averaged, to find the long-wave evolution equation:

$$\zeta_T = -\frac{1}{\epsilon}\left\langle \int_0^a \mathrm{d}r(J_X\cos\psi + \epsilon J_Y\sin\psi)\right\rangle \sim -\zeta_{XX}\langle aC(1-\nu C)\rangle$$
$$+\epsilon\left[\frac{1}{2}\zeta_{XXX}\langle a^2C^2\rangle + (\zeta_X^2)_X\left(\frac{1}{2}\langle aC\rangle\tan\phi + \mu\langle aC^2\rangle\right)\right]$$
$$-\epsilon^2\left[\frac{1}{4}(\zeta_X^2)_{XX}(\mu\langle a^2C^3\rangle + \langle a^2C^2\rangle\tan\phi) + \frac{1}{2}(\zeta_X^3)_X(\nu\langle aC^2\rangle - \langle aC\rangle) + \frac{1}{6}\zeta_{XXXX}\langle a^3C^3\rangle - \nu\zeta_{YY}\langle aS^2\rangle\right] \tag{26}$$

with several terms disappearing by virtue of the symmetry of the angular distribution.

Much of the dependence on the probability distributions can be further scaled out of the evolution equation by defining the new variables:

$$\zeta = Z\hat{\zeta}, \qquad X = Z\hat{X}, \qquad Y = \epsilon Z\hat{Y}\sqrt{\frac{\langle aS^2\rangle}{\langle aC^2\rangle}}, \qquad T = \frac{Z}{\langle aC\rangle}\hat{T}, \qquad \mu = \frac{\langle aC\rangle}{\langle aC^2\rangle}\hat{\mu}, \tag{27}$$

where $Z = \langle a^2C^2\rangle/\langle aC\rangle$. Then, after dropping the hat decoration:

$$\begin{aligned}\zeta_T \sim{}& (\mu\tan\phi - 1)\zeta_{XX} - \mu\zeta_{YY}\tan\phi + \tfrac{1}{2}\epsilon[\zeta_{XXX} + (2\mu + \tan\phi)(\zeta_X^2)_X] \\ &- \epsilon^2[\tfrac{1}{6}\beta_1\zeta_{XXXX} + \tfrac{1}{4}\beta_2(\zeta_X^2)_{XX} - \tfrac{1}{2}\beta_3(\zeta_X^3)_X],\end{aligned} \tag{28}$$

where

$$\beta_1 = \frac{\langle a^3C^3\rangle\langle aC\rangle}{\langle a^2C^2\rangle^2}, \qquad \beta_2 = \tan\phi + \mu\frac{\langle a^2C^3\rangle\langle aC\rangle}{\langle a^2C^2\rangle\langle aC^2\rangle}, \qquad \beta_3 = 1 - \mu\tan\phi. \tag{29}$$

Eq. (28) exposes the general form of the compact, long-wave model.

Formally speaking, the long-wave approximation is justified provided that the band of unstable wavenumbers is $k < \mathrm{O}(\epsilon)$, which places a certain constraint (easily derived from (21)) on the parameter settings. Equivalently, this requires that the wavelength of the most unstable ripples should be much greater than the reptation length. In fact, for typical parameter settings, the most unstable wavenumber is order one, and so the long-wave approximation is questionable. Nevertheless, we favour the long-wave theory because of its simplicity and the symmetries it captures, applying it in situations in which it may fail to give an accurate approximation of the integro-differential model. Note, in particular, that shadowing has been discarded in arriving at (28), which is appropriate near the onset of the instability and for small wavenumbers, but which may be the first approximation to fail.

## 5. One-dimensional ripples

### 5.1. Numerical results for the integro-differential model

In one dimension, the integro-differential equation (12) reduces to

$$\zeta_t = -\frac{\partial}{\partial x}\left[(1 - \mu\zeta_x)\int_0^\infty p(a)\,\mathrm{d}a\int_{x-a}^{x} F(x')\,\mathrm{d}x'\right]. \tag{30}$$

We solve this equation numerically, assuming periodic boundary conditions and using an explicit finite difference scheme. The step lengths are chosen from the exponential distribution, $p(a) = \mathrm{e}^{-a}$. To expedite comparison with experimental and observational data, we present the results in dimensional form. Time units are obtained by taking the saltation flux to be $N_{im}^0 = 10^7\,\mathrm{m}^{-2}\,\mathrm{s}^{-1}$, which, according to Anderson [14], is the saturated flux for a wind shear velocity of 0.5 m/s and for fine sand with grain diameter $d_s = 0.25$ mm. The mean step length is taken to be $\alpha = \bar{a} =$ 1 cm, which is close to the typical values reported by Andreotti et al. [32], and the impact angle is fixed as $\phi = 10^\circ$.

Fig. 5 shows the time evolution of the ripple pattern that emerges from random initial conditions. Ripples begin as small-amplitude perturbations or mottles on the surface (see Fig. 2 in [39]). The initial evolution of the slightly perturbed surface is dictated largely by linear theory, and the wavelength of the fastest linearly growing wave dominates the early stages of the evolution. The growing ripples remain almost symmetrical until nonlinear effects start to become significant. In cases in which the lee-slope angle exceeds the impact angle of the saltating grains, and shadowing becomes effective, the asymmetry becomes more marked and the downwind slope becomes yet steeper. In Fig. 6 we show a typical ripple profile after 10 min of evolution, illustrating how the different physical quantities are distributed along the ripple.

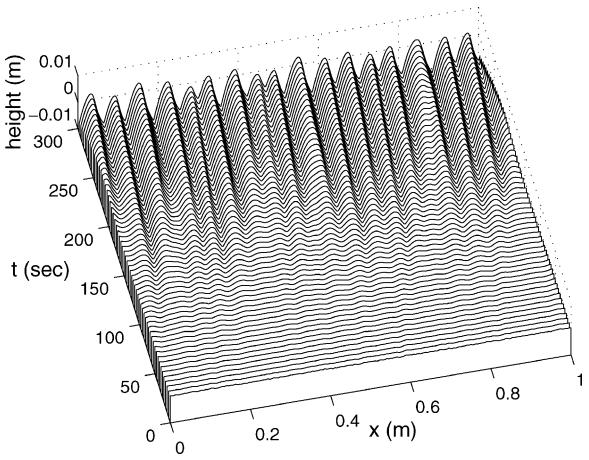


Fig. 5. Time evolution of the ripple pattern for $\mu = 0.9$ and constant impact angle $\phi = 10^\circ$. The ripples grow from low-amplitude, random initial perturbations. The drift velocity is approximately 1.2 cm/min, in agreement with field measurements [4] and with computer simulations [16]. The values of the other parameters are $N_{im}^0 = 10^7\,\mathrm{m}^{-2}\,\mathrm{s}^{-1}$ and $n = 2$.

Further development of the ripple pattern is due to a coarsening process, which noticeably increases the ripple wavelength (see Fig. 7). Small ripples travel faster than large-amplitude ripples [1], and collisions ensue wherein two ripples coalesce into a single larger ripple. Data from field observations [20] and from wind tunnel experiments [14] are consistent with an asymptotic power-law increase of the mean ripple wavelength, $\Lambda(t)$. Weakly nonlinear

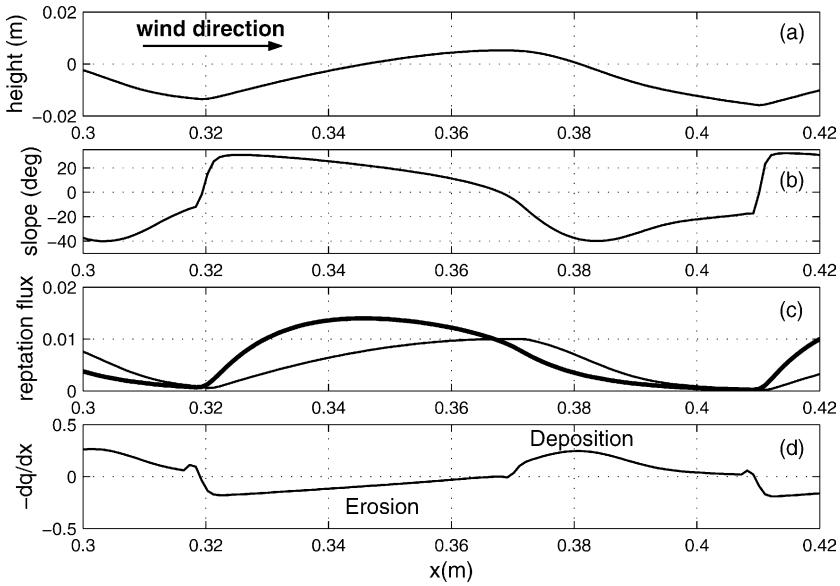


Fig. 6. A typical ripple profile for the parameter values $N_{im}^0 = 10^7\,\mathrm{m}^{-2}\,\mathrm{s}^{-1}$, $n = 2$, $\mu = 1.1$, $\phi = 10^\circ$ and $\bar{a} = 2$ cm. The ripple is depicted at time $t = 10$ min after the wind started blowing. (a) Elevation of the sand surface. The asymmetry in the ripple profile is mainly due to the shadowing effect. (b) Slope of the sand surface in degrees. (c) Reptation flux in $\mathrm{kg\,m}^{-2}\,\mathrm{s}^{-1}$. The thin line indicates the flux including the slope correction term and the thick line is the flux that would be met without the slope correction. (d) Spatial derivative of the reptation flux. Erosion (deposition) occurs for negative (positive) values. The windward side is eroded while the leeward side undergoes deposition; in this way the ripple travels downwind.

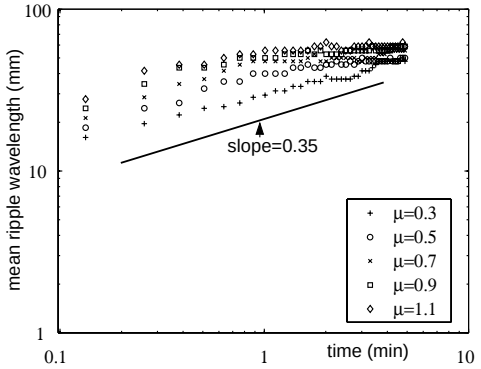


Fig. 7. Time evolution of the mean ripple wavelength for different values of $\mu$. At intermediate times the mean wavelength, $\Lambda(t)$, grows as a power-law, $\Lambda(t) \propto t^{\xi}$ with $\xi \approx 0.35$. The growth of the ripple wavelength becomes significantly slower at later times, and may end. The values of the other parameters are as in Fig. 5.

models [26,27] predict a similar behaviour, $\Lambda(t) \propto t^{\xi}$ with $0.27 < \xi < 0.5$. The data shown in Fig. 7 also suggest an initial power-law growth with $\xi \approx 0.35$. At later times, the ripple wavelength evolves more slowly and appears to saturate, although it is difficult to distinguish between saturation and a protracted logarithmic growth of $\Lambda(t)$ (which is expected from layer-interaction theories, see Elphick et al. [40] and Sun and Ward [41]).

The shape of the ripples predicted by the integro-differential model, as seen in Fig. 6, and the average ripple celerity compare qualitatively well with observations [7]. However, the stoss slope of the model ripples is slightly larger than the average values measured in the field, and the model ripple index is definitely smaller than that observed for real sand ripples. One heuristic way to generate model ripples with a larger index is to increase the value of $\mu$. Rather than proceeding with a parameter-fitting exercise, however, here we accept the existence of some discrepancy between model results and observed sand ripples and explore what are the possible origins of the problem.

As for the ripple profile, we note that there are at least two physical effects, not included in our simple approach, that could modify the value of the stoss slope. First, it was theoretically predicted by Rumpel [42] that saltation becomes energetically inefficient when the impact angle exceeds 15°. This suggests that the saltation flux will decrease as the stoss slope increases, leading to a dependence of $N_{im}^{0}$ on the local slope. Secondly, it can be argued that the number of reptating grains ejected upon impact should be smaller for the upwind slope than for the lee slope [32]. Thus, $n$ should also depend on the surface slope.

As for the difference in the ripple index, we recall that the value of the ripple index has been associated with the effects of shadowing [4], which is treated here in a simplified way. Shadowing effects are also mainly responsible for the asymmetry between the stoss and lee slopes of the ripples, which becomes more marked for large ripples where shadowing is more significant. Thus, an inadequate treatment of shadowing in our model could contribute both to the discrepancy in the ripple index and to the overly large stoss slopes. Future extensions of the modelling efforts should include a proper treatment of the non-local nature of shadowing.

### 5.2. Long-wave results

For one-dimensional ripples, we delete the term $\mu\zeta_{YY}\tan\phi$ from the long-wave model (28), leading to

$$\zeta_T \sim [(\mu\tan\phi - 1)\zeta_X + \tfrac{1}{2}\epsilon\zeta_{XX} + \tfrac{1}{2}\epsilon(2\mu + \tan\phi)\zeta_X^2 - \tfrac{1}{6}\epsilon^2\beta_1\zeta_{XXX} - \tfrac{1}{4}\epsilon^2\beta_2(\zeta_X^2)_X + \tfrac{1}{2}\epsilon^2\beta_3\zeta_X^3]_X. \tag{31}$$

Eq. (31) is similar to a model presented by Csahók et al. [26].

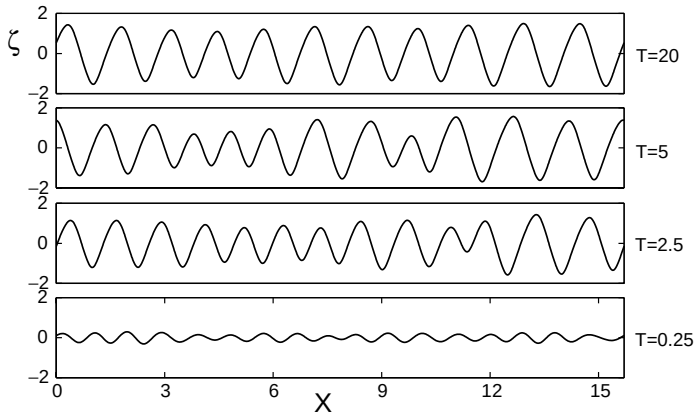


Fig. 8. Time evolution of the ripple field described by Eq. (31) for $\epsilon = \mu = 0.25$, $\phi = 10^\circ$, $\beta_1 = \beta_3 = 1$ and $\beta_2 = \tan\phi$, in a periodic domain of size $5\pi$.

We solve Eq. (31) numerically, by using an explicit fourth-order finite difference scheme and assuming periodic boundary conditions. For illustration, we fix $\epsilon = \mu = 0.25$, $\phi = 10^\circ$, $\beta_1 = \beta_3 = 1$ and $\beta_2 = \tan\phi$, and solve the equation in a periodic domain of size $5\pi$. The simulations begin from small random initial perturbations of the flat bed. Fig. 8 shows four snapshots of the ensuing ripple evolution.

The initial low-amplitude perturbations have an approximately flat power spectrum. When linear instability takes over, the spectrum becomes peaked at the wavelength of the most unstable mode (which has about 17 peaks in the domain). At later times, in the nonlinear regime, the mean wavelength grows as ripples merge in a coarsening process similar to that found for the integro-differential model; see Fig. 9. The time evolution of the power spectrum of the ripple field is shown in Fig. 10, together with the evolution of the wavelength of the dominant mode. Beyond $T = 10$, the coarsening of the pattern appears to end and the solution converges to a steady wavetrain that contains eleven ripples in the domain.

The presence of coarsening in the long-wave model is not surprising in view of the fact that Eq. (31) is a generalisation of the Cahn–Hilliard equation [28] (at least when expressed in terms of the surface gradient, $u =$

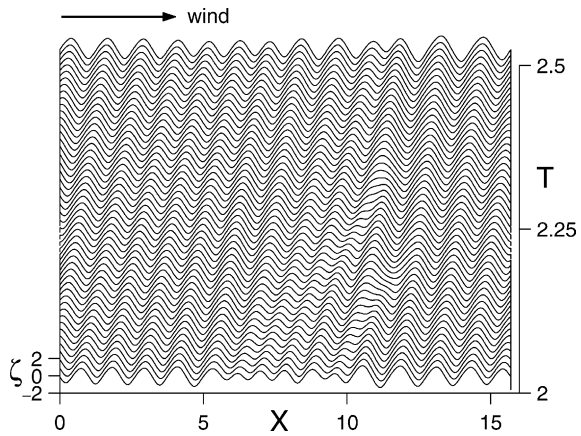


Fig. 9. Ripple evolution, according to Eq. (31), that shows the occurrence of merging events. This process leads to the increase of the mean ripple wavelength. Parameter values as in Fig. 8.

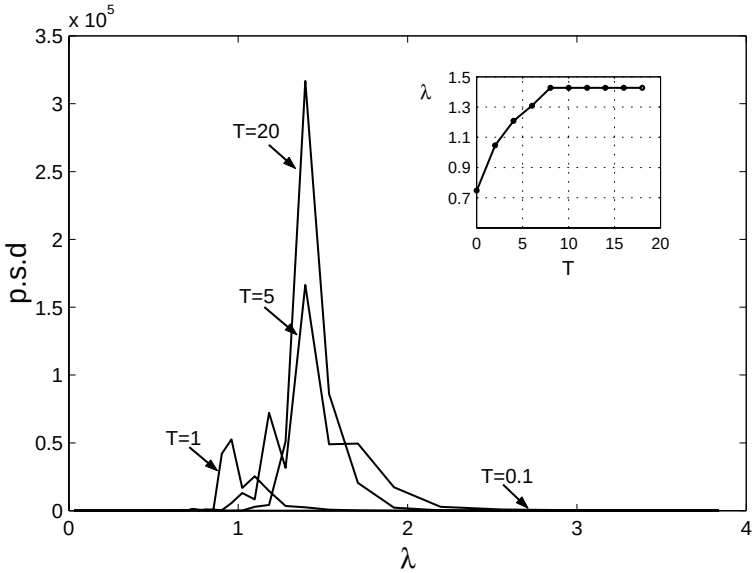


Fig. 10. Power spectra of the model ripples at different times, for the computation shown in Fig. 8. The initial low-amplitude perturbations have a flat power spectrum. During the nonlinear evolution, the mean ripple wavelength grows beyond the wavelength predicted by linear instability. The inset shows the time evolution of the mean ripple wavelength, $\lambda$.

$\zeta_X$). This latter equation has a Lyapunov functional and describes the evolution and coarsening of front patterns. Nevertheless, the presence of additional terms in Eq. (31) removes the Lyapunov functional, and so one cannot anticipate a coarsening dynamics without solving the equation. In fact, although the numerical solutions exhibit coarsening, they also indicate that ripple patterns coarsen for some time, but not indefinitely, in agreement with the simulations of the integro-differential equation (see also [26]). Thus, the inverse cascade becomes interrupted before it proceeds to its ultimate conclusion (a single ripple), which would be the prediction of Cahn–Hilliard. Another important difference between the current model and the Cahn–Hilliard equation arises from the lack of the inversion symmetry, $x \to -x$, which arises because here there is a preferred wind direction.

To explore the wavelength selection process in more detail, we have performed a suite of initial-value computations in varying domain size, $l$, beginning from low-amplitude, rapidly varying perturbations about the equilibrium state. The results are summarised in Fig. 11. The dominance of the linear instability in the first stage of evolution is indicated by the coincidence of the number of ripples in the first nonlinear structure with that expected from the most unstable linear eigenmode. Coarsening then reduces this number until the ripple pattern passes into a stability region which can be determined by computing the steady, propagating wave solutions and then testing their stability using Floquet theory (the shaded region in the figure is calculated in this way). The most common wavetrains have a ripple number that lies just below the upper boundary of the stability region, and, very roughly, are characterised by a wavelength of about 1.4. The corresponding wave heights are just below 3 units, implying a ripple index of $(2\epsilon)^{-1}$.

The stability region in Fig. 11 is wedge-shaped and is bounded from below by another curve, which is confirmed by a second type of initial-value computation in which the initial state consists of a slightly perturbed, steadily propagating pattern with a given number of ripples within each spatial period. In these other initial-value problems, the ripples can be too widely spaced to be stable, in which case disturbances grow in the gaps between ripples and ultimately spawn new ripples to decrease the wavelength.

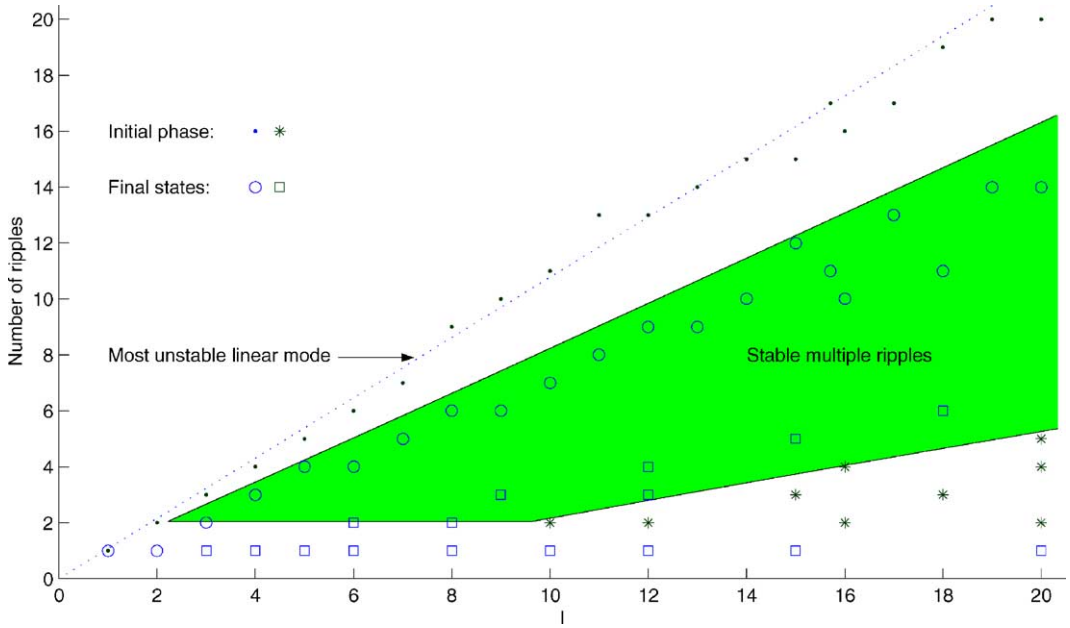


Fig. 11. Initial-value computations and stability regions on the (domain-size, ripple-number) plane. Shown are data from two types of initial-value problems. In the first, the initial state is a low-amplitude, rapidly varying profile. After a initial period, the system forms an unsteady train of relatively closely spaced ripples as indicated by the dots; subsequently, the pattern coarsens and eventually converges to the steady pattern represented by circles. In the second computations, the initial condition is close to a steady equilibrium computed from the periodic boundary-value problem for steadily propagating waves; some of these are stable, and the system persists in this state (squares), whereas others are unstable and the system evolves elsewhere (stars). Floquet stability computations of the steadily propagating nonlinear waves indicate the shaded stability region; the "fundamental" solution, containing a single ripple in the domain, appears to be always stable. Also displayed is the most unstable linear eigenmode.

Curiously, both the initial-value computations and the Floquet stability theory indicate that the longest wave in the domain is stable for all domain sizes considered. Thus, in addition to the wedge-shaped region of stable trains of multiple ripples, one can also find a stable "mega-ripple" with the size of the domain. However, trains of multiple ripples are selected far more commonly from arbitrary initial conditions. As the domain size increases, the longest waves limit to structures whose shape can be calculated analytically; the details are given in Appendix A, and can be used to estimate the limiting stoss and lee slopes, as well as the wavespeed, in terms of the system parameters. In particular, this analysis predicts that the stoss and lee slopes approach dimensionless constants determined by the system parameters, whereas the wavespeed varies inversely with the ripple spacing. The ripple height also varies linearly with wave spacing, implying a limiting ripple index of about $(2.6\epsilon)^{-1}$ for these large-amplitude solutions.

## 6. Two-dimensional ripple fields

Observations of aeolian ripples in deserts or on sandy beaches indicate that ripple fields are almost one-dimensional bedforms, and they display only small modulations in the direction transverse to the wind. Ripple crests run almost parallel to each other, with some sinuosity [7]. In well-developed ripple fields, the crests display bifurcation and defects (Y junctions), as shown in Fig. 1.

To our knowledge, the only theoretical models of two-dimensional ripple fields developed in past years were based on cellular automata (see, e.g., [16]). The main difficulty that is encountered in modelling two-dimensional ripple

fields is that there are no available experimental results on the angular form of the "splash function" [26,32,44]. Nevertheless, it is straightforward to build plausible distributions as in Section 2. To explore the two-dimensional dynamics, however, we do not use the integro-differential model, but instead we employ the long-wave equation, which does not rely on the detailed physical ingredients to the original theory.

We take $\epsilon = \mu = 0.25$, $\phi = 10^\circ$, $\beta_1 = \beta_3 = 1$ and $\beta_2 = \tan\phi$, and solve the long-wave model (28) numerically, beginning from low-amplitude, random initial conditions. The initial evolution is again dominated by the growth of the most unstable linear modes, and ripples appear in the form of small undulations on the sand surface. Once more, in the nonlinear regime, the ripple mean wavelength increases due to merging events, as shown in Fig. 12.

The ripple pattern initially develops dislocations (which are sometimes called "terminations" and "antiterminations" in the ripple literature [16]) which move laterally along the ripple crests. The dynamics of the model ripples is very similar to the behaviour of ripple bifurcations as recorded by sequential images of real sand surfaces [44]. Bifurcations move downwind from one ripple to the next, much faster than the ripples themselves. Fig. 13 shows a numerical simulation of the propagation of a defect through the ripple field.

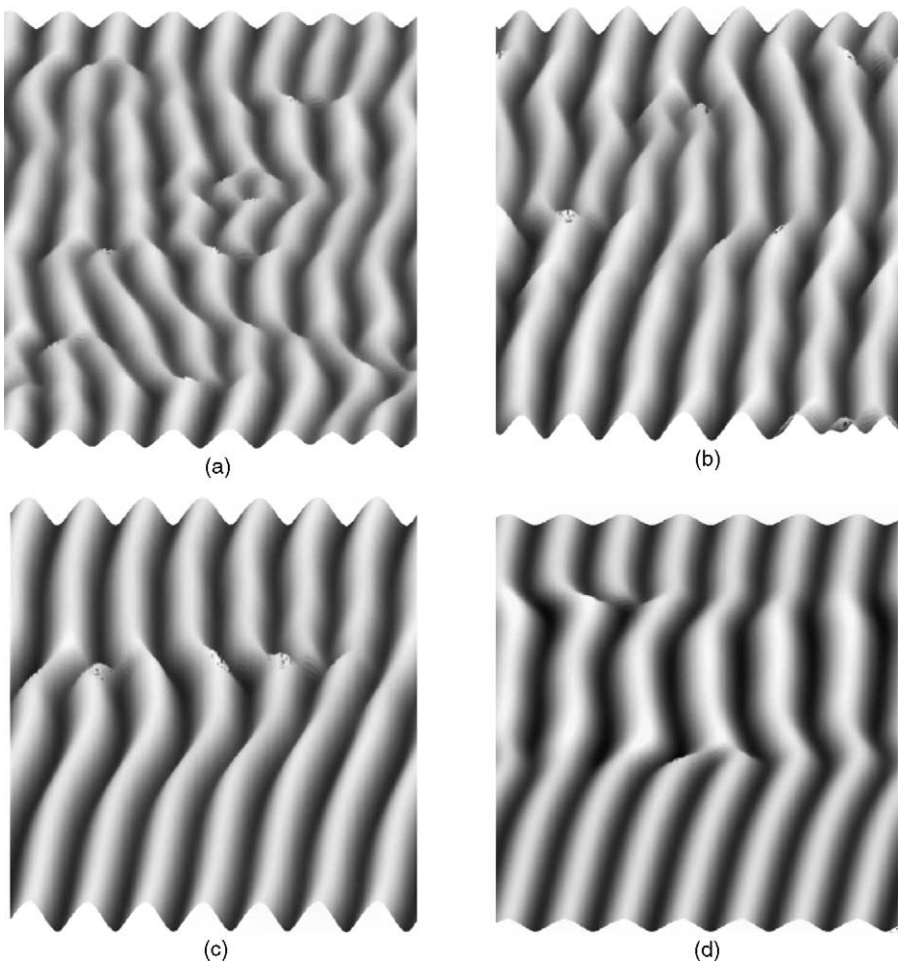


Fig. 12. Snapshots of a two-dimensional ripple field produced by the numerical integration of Eq. (28) on a $256 \times 256$ grid with periodic boundary condition, at $T = 2, 4, 8, 16$. The wind direction is from left to right. Parameter values: $\epsilon = \mu = 0.25$, $\phi = 10^\circ$, $\beta_1 = \beta_3 = 1$, $\beta_2 = \tan\phi$ and a domain size of $5\pi/2$.

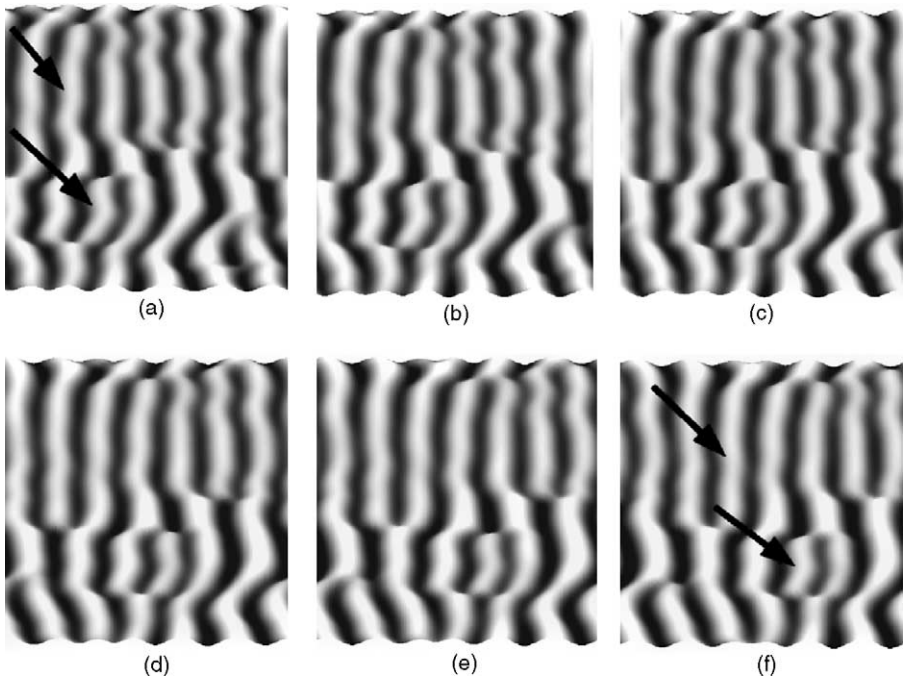


Fig. 13. This sequence of frames shows the ripple field at time intervals spaced by $\Delta T = 0.05$ for $\epsilon = \mu = 0.3$, $\phi = 10^\circ$, $\beta_1 = \beta_3 = 1$ and $\beta_2 = \tan\phi$. The first frame is at $T = 1.55$. The defect advances from one ripple to the next much faster than the ripples. The two arrows in frames (a) and (f) show the instantaneous location of one ripple and of the defect. A similar pattern can be seen in the natural ripple fields of Fig. 1. As the defect gets closer to the next ripple, it triggers a detachment of another defect, which advance further, while the original defect merge into the ripple. This scenario continues while the defect crosses the field of ripples.

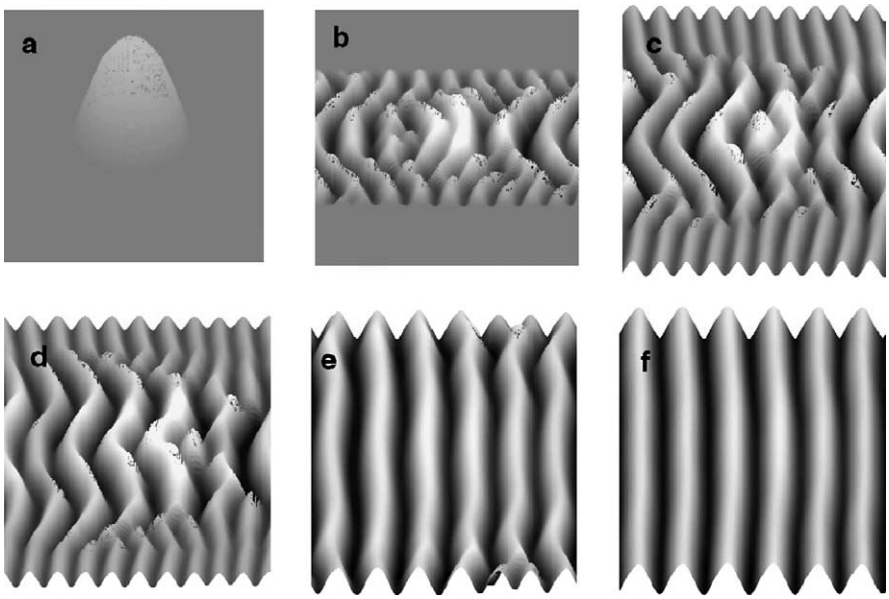


Fig. 14. Plan view of simulated ripples initiated from a sand pile, on a $256 \times 256$ grid for $\epsilon = \mu = 0.2$, $\phi = 10^\circ$, $\beta_1 = \beta_3 = 1$ and $\beta_2 = \tan\phi$, The first panel shows the initial sand pile. The last panel is at $T = 16$.

The evolution of ripples emerging from an isolated perturbation provides further insight on how ripples organise themselves in the cross-wind (lateral) direction. Fig. 14 shows a numerical integration from an initial condition in the form of a small Gaussian hump. After a short time, the initial pile generates an array of ripples. Note that because of the periodic boundary conditions, when the ripples cross the right edge of the simulation box, they re-enter from the left side. During the evolution, the ripples spread laterally and the crests tend to become parallel, indicating stability with respect to perturbations in the transverse direction.

At the beginning of the evolution, there is a significant difference between the central portion of the domain, where the ripples develop directly from the initial sand pile, and the parts of the domain where the ripples were generated by lateral diffusion of the initial perturbation. As time proceeds, merging processes take place and the ripple wavelength increases. The merging and lateral diffusion also act to decrease the differences between the various portions of the domain. This general pattern is similar to that found for ripples formed from an initial mound of sand under water in a flume [45], and to that obtained by integrating a cellular-automaton model [16].

## 7. Discussion and conclusions

In this work we have discussed a continuum model describing the dynamics of two-dimensional aeolian sand ripples. The theory is based on the idea that the ripple instability is generated by the positive feedback between undulations of the sand bed and the spatial variability of the flux of reptating grains. The model is formulated in terms of an integro-differential equation and extends the work of Anderson [13] by adding the third spatial dimension and a physically motivated flux correction that makes the reptation flux decrease on the windward slope of the ripples and increase on the lee slope. Similar slope-dependent corrections are used to regularise models of fluvial bedforms which display linear growth rates that diverge with wavenumber (see e.g. [46]).

A long-wavelength approximation to the integro-differential model leads to a generic nonlinear amplitude equation (31) which bears some resemblance to the Cahn–Hilliard equation. In one dimension, the long-wave theory appears to capture the same nonlinear dynamics as the original integro-differential model. In two dimensions, the long-wave model predicts that nonlinear ripples undergo a coarsening process, drift downwind, and show a pattern of mobile defects which move from one ripple to another, as observed for natural sand ripples [44].

Nevertheless, although our solutions share many common features with observed ripples, we have sedulously avoided a detailed comparison between theory and observations on the grounds that this would amount to an exercise in parameter fitting. Indeed, we have verified that we can tune parameters to bring the theory more in line with observations of, for example, ripple wavespeeds and indices. In view of the crudeness of the model, and the questionable significance of the parameter fit, we have not proceeded in that direction. Instead, our main focus has been a qualitative discussion of the dynamics of the model in both one and two dimensions. In particular, we offered a detailed description of coarsening in one dimension, and illustrated pattern dynamics in two dimensions. We hope this discussion motivates further work, both experimental and observational.

Given the track we have taken, one is naturally lead to ask whether there are qualitative disagreements between the predictions of the model and observations. Two points of disagreement present themselves immediately. First, it is observed that ripples disappear in strong winds. In our model, the wind speed appears only indirectly through the constant $Q_0$ used to remove the time dimension. Thus, the disappearance of ripples at high wind speed is not captured, and further extensions are required.

Second, the model cannot account for large amplitude bedforms. In the models discussed here we have assumed the saltation flux to be uniform. However, large enough undulations of the bed will break this ideal picture of a uniform saltation flux. In such cases, the saltation flux can depend on the bed topography, similarly to what has

been discussed here for the reptation flux. This may explain the formation of large-scale ripples, whose dominant wavelength can depend on the mean saltation length as suggested by Ellwood et al. [47]. In this case, the Exner equation must also include the spatial variability of the saltation flux:

$$(1-\lambda_p)\rho_p\frac{\partial\zeta}{\partial t} = -(\nabla\cdot\mathbf{Q}_s + \nabla\cdot\mathbf{Q}_r), \tag{32}$$

where $\nabla\cdot\mathbf{Q}_s$ dominates on large scales while $\nabla\cdot\mathbf{Q}_r$ dominates on small scales. Such a two-scale model may explain the fact that sometimes small ripples are superimposed on larger ones (see Fig. 5 in [47]). This is one direction along which the model discussed here can be extended [48].

## Appendix A. The profile of the limiting, long-wave ripple

In long-wave theory, the profile and speed of very wide ripples can be built by asymptotic means. The first relevant observations are that $c \sim L^{-1} \ll 1$, where $L$ is the ripple separation, and the ripple shape, described in terms of the surface slope $u = \zeta_x$, develops wide, smoothly varying sections separated by sharp transition layers; see Fig. 15. With $u = U(x-ct) \equiv U(\xi)$, the equation to be satisfied is

$$cU - (1-\mu\tan\phi)U_\xi + \tfrac{1}{2}\epsilon U_{\xi\xi} - \tfrac{1}{6}\epsilon^2 U_{\xi\xi\xi} + \tfrac{1}{2}\epsilon(2\mu+\tan\phi)(U^2)_\xi - \tfrac{1}{4}\epsilon^2\beta_2(U^2)_{\xi\xi} + \tfrac{1}{2}\epsilon^2(U^3)_\xi = 0, \tag{A.1}$$

where $\xi = x - ct$ is a travelling-wave coordinate, and for simplicity we have set $\beta_1 = \beta_3 = 1$.

The asymptotic construction proceeds by matched asymptotic expansion: we first build the smoothly varying sections over a relatively long, "outer" regions. Here, it is convenient to rescale the independent coordinate: $X = c\xi$. Then, to leading order in $c$:

$$U - (1-\mu\tan\phi)U_X + \tfrac{1}{2}\epsilon(2\mu+\tan\phi)(U^2)_X + \tfrac{1}{2}\epsilon^2(U^3)_X \sim 0, \tag{A.2}$$

which can be integrated to provide the implicit solution:

$$X(U) \sim X_0 + (1-\mu\tan\phi)\log|U| - \epsilon(2\mu+\tan\phi)U - \tfrac{3}{4}\epsilon^2U^2, \tag{A.3}$$

where $X_0$ is a constant of integration. This provides the profile of the long smooth sections of the ripple profile, as shown by dotted lines in Fig. 15. The sections begin at the termination of one of the transition layers, labelled $U_1$ and

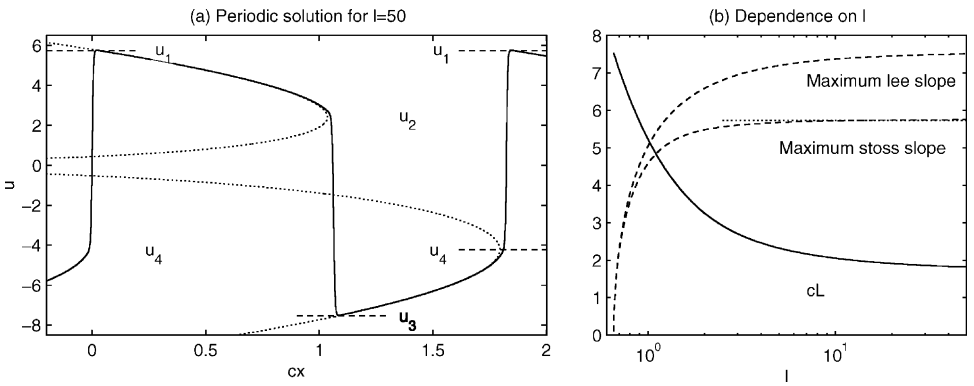


Fig. 15. Panel (a): limiting, steady ripple solutions and their asymptotic construction. Panel (b) shows how the wavespeed and the maximum stoss and lee slopes limit to the asymptotic values predicted in this appendix. Parameter choices as in the main text.

$U_3$, travel along two of the branches defined by (A.3), and then end in another transition layer at the terminations of the solution branches, labelled $U_2$ and $U_4$. The latter are defined by

$$U_{2,4} = \frac{1}{3}\epsilon\left[-(2\mu + \tan\phi) \pm \sqrt{4\mu^2 + \tan^2\phi + 6 - 2\mu\tan\phi}\right]. \tag{A.4}$$

Within the sharp, "inner," transition layers, we return to the system defined with coordinate $\xi$. To leading order, we find an oscillator equation:

$$\frac{1}{6}\epsilon^2 U_{\xi\xi} + \frac{\mathrm{d}V}{\mathrm{d}U} \sim \frac{1}{2}\epsilon U_\xi - \frac{1}{4}\beta_2\epsilon^2 (U^2)_\xi \tag{A.5}$$

with a negative damping and potential, $V(U)$, given by

$$\frac{\mathrm{d}V}{\mathrm{d}U} = K + (1 - \mu\tan\phi)U - \tfrac{1}{2}\epsilon(2\mu + \tan\phi)U^2 - \tfrac{1}{2}\epsilon^2 U^3 \equiv K + F(U), \tag{A.6}$$

where $K$ is another constant of integration. The inner solution, the transition layer, connects the equilibrium points defined by (A.6). To match with the outer solution, these equilibria must also be the pairs, $(U_4, U_1)$ or $(U_2, U_3)$. Thus, $F(U_1) = F(U_4)$ and $F(U_2) = F(U_3)$, which defines

$$U_{1,3} = \frac{1}{3\epsilon}\left[-(2\mu + \tan\phi) \pm 2\sqrt{4\mu^2 + \tan^2\phi + 6 - 2\mu\tan\phi}\right] \tag{A.7}$$

and provides the maximum upwind and downwind slopes of the ripple. At this stage, it is not necessary to further integrate (A.6) unless one wishes to construct the detailed structure of the transition layer.

Finally, the length of the orbit can be found from the outer solution:

$$cL \sim X(U_2) - X(U_1) + X(U_4) - X(U_3). \tag{A.8}$$

The asymptotic predictions for the maximum stoss and lee slopes, $U_1$ and $-U_3$, and the wavespeed, $c$, are shown in Fig. 15, and compared to numerical data.

## References


[1] R.A. Bagnold, The Physics of Blown Sand and Desert Dunes, Methuen, 1941.
[2] R. Greeley, et al., J. Geophys. Res. 107 (E1) (2002).
[3] S.H. Williams, et al., Lunar Planet. Sci. XXXIII (2002).
[4] R.P. Sharp, J. Geol. 71 (1963) 617.
[5] I.G. Wilson, Sedimentology 19 (1972) 173.
[6] K. Pye, H. Tsoar, Aeolian Sand and Sand Dunes, Unwin Hyman, London, 1990.
[7] R. Cooke, A. Warren, A. Goudie, Desert Geomorphology, UCL Press, London, 1993, Chapter 19.
[8] N. Lancaster, Geomorphology of Desert, Routledge, New York, 1995.
[9] J.D. Walker, An experimental study of wind ripples, Master Thesis in Geology, MIT, 1981.
[10] J.F. Kennedy, Ann. Rev. Fluid Mech. 1 (1969) 147.
[11] F. Brugmans, Earth Surf. Proc. Landforms 8 (1983) 527.
[12] M. Matchinski, La Nature 3241 (1955) 169.
[13] R.S. Anderson, Sedimentology 34 (1987) 943.
[14] R.S. Anderson, Earth Sci. 29 (1990) 77.
[15] B.B. Willetts, M.A. Rice, Earth Surf. Proc. Landforms 14 (1989) 719.
[16] W. Landry, B.T. Werner, Physica D 77 (1994) 238.
[17] L. Prigozhin, Phys. Rev. E 60 (1999) 729.
[18] J. Hardisty, R.J.S. Whitehouse, Nature 332 (1988) 532.
[19] H. Nishimori, N. Ouchi, Phys. Rev. Lett. 71 (1993) 197.
[20] B.T. Werner, D.T. Gillespie, Phys. Rev. Lett. 71 (1993) 3230.

[21] R.B. Hoyle, A. Woods, Phys. Rev. E 56 (1997) 6861.
[22] O. Terzidis, et al., Eur. Phys. J. B 5 (1998) 245.
[23] R.B. Hoyle, A. Mehta, Phys. Rev. Lett. 83 (1999) 5170.
[24] A. Valance, F. Rioual, Eur. Phys. J. B 10 (1999) 543.
[25] Z. Csahók, et al., Physica D 128 (1999) 87.
[26] Z. Csahók, et al., Eur. Phys. J. E 3 (2000) 71.
[27] H.A. Makse, Eur. Phys. J. E 1 (2000) 127.
[28] N.J. Balmforth, et al., in: N.J. Balmforth, A. Provenzale (Eds.), Geomorphological Fluid Mechanics, Springer, Berlin, 2001.
[29] T.-D. Miao, et al., Phys. Lett. A 288 (2001) 16.
[30] C. Misbah, A. Valance, Eur. Phys. J. E 12 (2003) 523.
[31] J.-P. Bouchaud, M.E. Cates, J.R. Prakash, S.F. Edwards, J. Phys. France I 4 (1994) 1383.
[32] B. Andreotti et al., Phys. J. B 28 (2002) 321.
[33] A. Fowler, in: N.J. Balmforth, A. Provenzale (Eds.), Geomorphological Fluid Mechanics, Springer, Berlin, 2001.
[34] G. Sauermann, K. Kroy, H.J. Herrmann, Phys. Rev. E 64 (2001) 31305.
[35] J. Ungar, P.K. Haff, Sedimentology 34 (1987) 289.
[36] B.T. Werner, J. Geology 98 (1990) 1.
[37] S.B. Forrest, P.K. Haff, Science 255 (1992) 1240.
[38] P.K. Haff, R.S. Anderson, Sedimentology 40 (1993) 175.
[39] I.K. McEwan, et al., Sedimentology 39 (1992) 971.
[40] C. Elphick, E. Meron, E.A. Spiegel, SIAM J. Appl. Math. 50 (1990) 490.
[41] X.D. Sun, M.J. Ward, Studies Appl. Math. 105 (2000) 203.
[42] D.A. Rumpel, Sedimentology 32 (1985) 267.
[43] R.S. Anderson, K.L. Bunas, Nature 365 (1993) 740.
[44] R.S. Anderson, R.R. McDonald, Eos 71 (1990) 1344.
[45] J.B. Southard, J.R. Dingler, Sedimentology 16 (1971) 251.
[46] J. Fredsoe, J. Fluid Mech. 64 (1974) 1.
[47] J.M. Ellwood, et al., J. Sedimentol. Petrol. 45 (1975) 554.
[48] H. Yizhaq, Physica A, in press.